Proposal for detecting degenerate bands with topological invariants in optical lattices

Jing-Xin Liu [1,2,*] Jian-Te Wang [1,2] and Hai-Tao Ding [1,2,3,†]

[1] *National Laboratory of Solid State Microstructures and School of Physics, Nanjing University, Nanjing 210093, China*

[2] *Key Laboratory of Atomic and Subatomic Structure and Quantum Control (Ministry of Education), Guangdong Basic Research Center of Excellence for Structure and Fundamental Interactions of Matter, School of Physics, South China Normal University, Guangzhou 510006, China*

[3] *Department of Physics, National University of Singapore, Singapore 117551*

(Received 11 March 2024; accepted 7 June 2024; published 26 June 2024)

In this paper, we present an experimental approach for simulating and detecting topological invariants using ultracold fermions confined in two-dimensional hexagonal optical lattices. We propose achieving degenerate four-band models with nontrivial topologies in both the AII and A classes by introducing additional inertial forces, Raman processes, or periodic driving. By implementing various quench sequences and observing the evolution of the time-of-flight pattern, we can gather comprehensive information about the ground states and determine the topological property of the valence bands. Through the analysis of tomographic results, we are able to extract and calculate the spin Chern number. Additionally, we demonstrate the robustness of the quantized topological invariants and discuss the effects of various experimental parameters.

DOI: 10.1103/PhysRevA.109.063332

I. INTRODUCTION

The discovery of the quantum spin Hall (QSH) effect in materials with strong spin-orbit coupling (SOC) has led to the emergence of a new class of topological states called $\mathbb{Z}_2$ topological insulators [1–3]. With advancements in experimental techniques, researchers can now investigate quantum phenomena in artificial systems such as Rydberg-excited atoms [4], trapped ions [5,6], superconductor circuits [7], and nanostructured materials [8]. These platforms offer a unique opportunity to explore the quantum behaviors of matter and their potential applications in quantum information processing.

Studies of topological effects often require ultrastrong gauge fields or spin-orbit couplings. Cold atoms confined in optical lattices provide an excellent platform for emulating a wide range of systems in condensed matter physics [9–11]. Synthetic gauge fields and SOC can be realized using various techniques, including trap rotation [12], microrotation [13–17], and Raman laser-induced transitions [18–30]. By combining laser-induced tunneling and superlattice techniques, strong Abelian [26] and non-Abelian [24] gauge fields can be achieved, enabling the simulation of topological insulators and other models. These technologies have been proposed for realizing quantum Hall and quantum spin Hall states [27–37].

The discovery of topological matters has opened up new avenues for quantum control and measurement. The probing techniques for different topological phase are also important for quantum simulation. These techniques can be divided into two main types. The first type involves directly extracting the topological properties locally, such as extracting the Berry curvature of the entire Brillouin zone (BZ), which can be achieved using interferometers [38–42], studying the semiclassical dynamics of wave packets [43–46], or using a phase-retrieval algorithm [47]. The quantum state tomography method which measure the entire BZ can also be viewed as a measure interference pattern from the time-of-flight (ToF) image [35,48]. Several experiments concerning the tomography of two-level models in cold-atom systems have been realized based on the dynamics after different quench sequences [49–51], projection on different momenta by fast acceleration [52], and off-resonant coupling to higher bands [53]. As for the second type, these involve directly detecting physical observables that act as a response to the topological phase or topological invariants, such as density profile plateaus from the Streda formula [32,54–60] or edge states detected using Bragg spectroscopy [61–67]. All of these techniques are being used to study topological phases of matter in artificial systems and to explore their potential applications in quantum technology.

To date, many experimental works on simulating the lattice Chern insulator models have been realized on ultracold-atom platforms. This means that simple quantum simulation techniques using cold atoms are becoming mature. Therefore, we aim to explore topological insulators with additional symmetries. If we consider the case with time-reversal symmetry (TRS) and other symmetry, the lattice model is complicated for realization. Optical lattice systems have been used to realize models with both TRS and nontrivial topology. This has been achieved through the application of gradient magnetic fields and Raman laser fields [37,68,69]. However, realization of nontrivial topology and breaking of spin conservation simultaneously remains a challenge. In this paper, we propose

*Contact author: 602023220045@smail.nju.edu.cn

†Contact author: hiding@smail.nju.edu.cn

the realization of a hexagonal geometric structure that exhibits nontrivial topology in twofold degenerate four-band models. In our first model, we introduce additional inertial forces and Raman fields to achieve a nontrivial phase belonging to class AII with additional s_x spin symmetry. In the second model, we combine two Haldane models with opposite Chern numbers and introduce terms that preserves degeneracy while breaking spin conservation. We can still define the spin-Chern number (SCN) for such a system when s_z spin conservation and TRS are broken, and we present an experimental scheme to simulate and probe these topological invariants. Our proposal involves trapping cold atoms in a two-dimensional (2D) spin-dependent optical lattice subjected to periodic driving and modulation. We aim to measure the topology of the degenerate bands through the evolution of ToF images with quench dynamics.

The paper is organized as follows. Section II provides a definition of SCN. In Sec. III, we discuss the realization of the topological phase of a four-band model in class AII and class A with twofold degeneracy. In Sec. IV, we introduce a method for band tomography by analyzing ToF images with the aid of quench dynamics. This method allows for the direct calculation of the spin Hamiltonian and Berry curvature of the entire BZ in the spin nonconserving case, thereby obtaining the topological invariants. Finally, Sec. V provides a discussion about experimental parameters and the conclusion of the paper.

II. QUANTUM SPIN HALL EFFECT MODEL AND SPIN CHERN NUMBER

In the study of topological insulators within the AII class, the system's behavior is typically characterized by $\mathbb{Z}_2$ topological invariants [70]. When additional symmetries like spin conservation (s_z) are introduced, the classification shifts from $\mathbb{Z}_2$ to $\mathbb{Z}$. In such cases, the SCN can be defined based on the differences in Chern numbers between distinct spin components. Even without spin conservation, as explored in Refs. [71,72], the SCN remains applicable. In these situations, the expected spin values for the two valence bands do not simply fall at -1 and $+1$, but form distinct regions. As long as these differences remain discernible, the edge states can be viewed as clusters with different spin orientations.

To determine the SCN, researchers employ a method that involves decomposing the occupied valence bands into two sectors by diagonalizing the expression $\hat{P}\hat{s}_z\hat{P}$, where $\hat{P}$ represents the valence band projection operator. This diagonalization allows us to represent $\hat{P}\hat{s}_z\hat{P}$ as a 2×2 matrix $\langle u_\alpha(k)|\,\hat{s}_z\,|u_\beta(k)\rangle$ within the valence band. To compute the SCN, we calculate the spin Berry curvature $\mathcal{F}_\pm(k) = i\varepsilon_{\mu\nu}\,\langle\partial_\mu\psi_\pm(k)|\partial_\nu\psi_\pm(k)\rangle$, where $\pm$ represent two orthogonal degenerate sectors. Using this, we define $C_\pm = 1/(2\pi)\int \mathrm{d}^2k\mathcal{F}_\pm(k)$ and define $C_s = C_+ - C_-$ [73]. It has been proven that this method remains robust against continuous deformations of the system Hamiltonian, including symmetry-breaking perturbations, as shown in Refs. [74,75]. Using this method, the SCN can also be defined when TRS is broken [76], and there exists QSH effect but without Kramer pairs. In the next section, we will introduce two models that can be realized in an optical lattice with ultracold Fermi gas, following the idea of SCN described above.

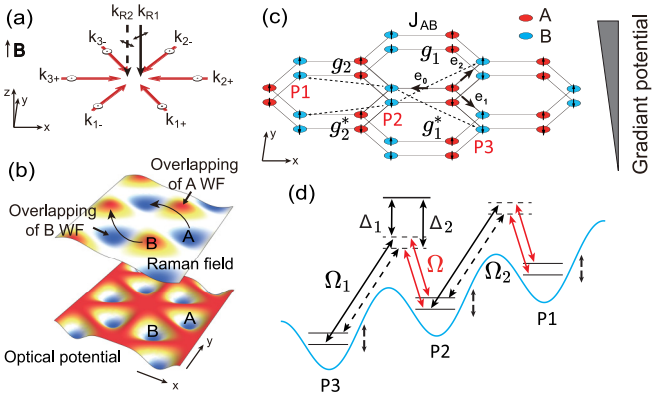

FIG. 1. (a) The laser configuration for the two-dimensional hexagonal optical lattice. (b) The hexagonal optical potential and Raman field $\mathbf{M}(\mathbf{r})$. The overlapping region of Wannier functions indicates that the Raman process takes opposite values for different sublattices. (c) The tight-binding model of this system, with some spin-flip hopping indicated by black dashed arrows. (d) Spin-flip hopping in the optical lattice tilted by an additional gradient potential. Two laser fields (black solid and dashed arrows) match the frequency difference of spin-flip hopping along different directions.

III. REALIZATION IN OPTICAL LATTICE

We present two possible approaches for realizing and detecting nontrivial topology with twofold degeneracy. The first model presents a method to realize a system that maintains TRS($\mathcal{T}^2 = -1$) in the AII class with s_x conservation, without introducing additional SOC. The second model is based on two Haldane models with opposite Chern numbers. We also introduce additional terms to break spin conservation while maintaining the condition of the double global degeneracy. All of these models could exhibit nontrivial topological invariants.

A. Model 1: AII class with s_x conservation

In this section, we discuss the realization of a model with TRS ($\mathcal{T}^2 = -1$) and conserved s_x. The model's topological invariant is SCN, which falls under $\mathbb{Z}$ classification. The implementation of a $\mathcal{T}$-symmetric model has been achieved in an optical lattice by incorporating gradient magnetic and Raman laser fields [37,68,69,77]. A similar strategy could be applied on honeycomb lattice. However, the difference in our scheme is that in order to realize the topological phase, an additional external force should be introduced.

An optical potential can be generated using six laser fields with wave vectors $\mathbf{k}_{i\pm}$ and polarization along $\hat{z}$, as illustrated in Fig. 1(a) with red arrows. By carefully choosing frequencies for extra laser fields propagating along the $\hat{z}$ direction, we establish additional two-photon Raman processes. This mechanism facilitates the coupling of different spins at specific positions with two different Raman fields.

The complete Hamiltonian encompasses the optical potential $V(\mathbf{r})$ and Raman fields $\mathbf{M}_1(\mathbf{r})$, $\mathbf{M}_2(\mathbf{r})$, taking into account the influence of the Zeeman field and external force in the

Raman field:

$$H = \frac{\mathbf{p}^2}{2m_0} + V(\mathbf{r}) + \mathbf{M}_1(\mathbf{r}) \cdot \boldsymbol{S} + \mathbf{M}_2(\mathbf{r}) \cdot \boldsymbol{S}. \quad (1)$$

The optical potentials are formed by laser fields with wave vectors $\mathbf{k}_{i\pm} = \sqrt{3}R_z(\pm\pi/6)\mathbf{k}_i$, where $\mathbf{k}_1 = (0, 1, 0)$, $\mathbf{k}_2 = (-\sqrt{3}/2, -1/2, 0)$, $\mathbf{k}_3 = (\sqrt{3}/2, -1/2, 0)$, and $R_z(\theta)$ is the rotation operator along the z axis. The combined electric field of all laser fields propagating in the x–y plane is

$$\mathcal{E}(\mathbf{r}) = E_0 \sum_{j=1}^{3} [\exp(-i\mathbf{k}_{j+} \cdot \mathbf{r}) - \exp(-i\mathbf{k}_{j-} \cdot \mathbf{r})]\mathbf{e}_z, \quad (2)$$

where lasers with opposite wave vectors exhibit an additional π phase difference. The associated optical potential is given by $V(\mathbf{r}) = -\alpha_s|\mathcal{E}(\mathbf{r})|^2$, as depicted in Fig. 1(b), where α_s represents the atomic polarizability and E_0 represents the strength of the electric field.

With the help of Raman fields, the inertial force generated by accelerating the lattice in a specific direction facilitates the coupling of spins at particular positions. The Zeeman field introduces an energy difference, allowing for the independent coupling of different spins. By carefully choosing the frequency of laser fields $\mathcal{E}_{R1}(\mathbf{r})$ and $\mathcal{E}_{R2}(\mathbf{r})$ in Fig. 1(a) with solid and dashed black lines propagating along the $\hat{z}$ direction, we can control the next-nearest-neighbor (nNN) spin-flip hopping independently. The laser fields $\mathcal{E}_{R1}(\mathbf{r})$ and $\mathcal{E}_{R2}(\mathbf{r})$ are considered constant at the $z = 0$ plane. By adjusting the polarization of these laser fields, we can introduce σ_+ or σ_- processes independently. For instance, in Fig. 1(d), the red arrows represent the π transition process, while the black solid and dashed lines depict the σ_+ and σ_- transitions, discernible through the changes in spin.

The determination of tight-binding parameters relies on the analysis of Wannier-Stark functions in the presence of gradient field caused by inertial force. The terms governing nNN spin-flip hopping are associated with the overlap of two distinct Wannier-Stark functions with different spins on the same sublattice. Therefore, an analysis of the Raman field properties is crucial. The Rabi frequencies Ω, Ω_1, and Ω_2 in Fig. 1(d) are proportional to $\mathcal{E}(\mathbf{r})$, $\mathcal{E}_{R1}(\mathbf{r})$, and $\mathcal{E}_{R2}(\mathbf{r})$. Consequently, the Raman field term can be expressed as $\mathbf{M}_1(\mathbf{r}) = \Omega_1^*(\mathbf{r})\Omega(\mathbf{r})/\Delta_1\hat{S}^- + \text{H.c.}$, as shown in Fig. 1(b), representing the coupling between $|\uparrow\rangle$ at P2 and $|\downarrow\rangle$ at P3 in Fig. 1(d). Similarly, coupling in the opposite direction is achieved by the Raman field $\mathbf{M}_2(\mathbf{r}) = \Omega_2(\mathbf{r})\Omega^*(\mathbf{r})/\Delta_2\hat{S}^- + \text{H.c.}$. The detunings Δ_1 and Δ_2 are the effective frequency differences between the D line and the π polarization laser's frequency for different spins (magnetic subenergy levels in the hyperfine structure) in Fig. 1(d). The actual contributions should sum all possible two-photon Raman processes in the D_1 and D_2 lines. Therefore, Δ_1 and Δ_2 are only effective values corresponding to these actual processes.

Observing the Raman field values in Fig. 1(b), it becomes apparent that nNN spin-flip hopping takes opposite values on different sublattices. The nNN spin-flipping terms along the y direction, induced by the Raman process, can be disregarded due to the antisymmetric structure of the Raman field $\mathbf{M}(\mathbf{r})$ relative to the middle of the A-B sublattice. Consequently, we can formulate the tight-binding Hamiltonian as depicted in Fig. 1(c),

$$\hat{H}_{tb} = \sum_{\langle \mathbf{r},\mathbf{s}\rangle,\sigma} J_{AB} a^\dagger_{\mathbf{r},\sigma} b_{\mathbf{s},\sigma} + \sum_{\langle\langle \mathbf{r},\mathbf{s}\rangle\rangle} \big(g_1 a^\dagger_{\mathbf{r},\downarrow} a_{\mathbf{s},\uparrow} + g_2 a^\dagger_{\mathbf{r},\uparrow} a_{\mathbf{s},\downarrow} - g_1 b^\dagger_{\mathbf{r},\downarrow} b_{\mathbf{s},\uparrow} - g_2 b^\dagger_{\mathbf{r},\uparrow} b_{\mathbf{s},\downarrow}\big) + \text{H.c.}, \quad (3)$$

using annihilation operators $\hat{a}_{\mathbf{r},\sigma}/\hat{b}_{\mathbf{r},\sigma}$ for particles at sublattice A/B with spin σ and position $\mathbf{r}$. Here, $\langle \mathbf{r}, \mathbf{s}\rangle$ calculates all nearest-neighbor (NN) terms, and $\langle\langle \mathbf{r}, \mathbf{s}\rangle\rangle$ calculates the four possible nNN hopping terms in Fig. 1(c). The SOC terms $g_j \propto \Omega_j\Omega^*$ illustrate that these terms can be controlled independently by adjusting the amplitude and phase difference of $\mathcal{E}_{R1}$ and $\mathcal{E}_{R2}$. By setting $g_1 = g_2 = ig$, the Bloch Hamiltonian is

$$H(\mathbf{k}) = B_x(\mathbf{k})\sigma_x + B_y(\mathbf{k})\sigma_y + B_{xz}(\mathbf{k})s_x\sigma_z, \quad (4)$$

where

$$B_x = \text{Re}\left[\sum_j J_{AB,j} \exp(-i\mathbf{k} \cdot \mathbf{e}_j)\right],$$

$$B_y = \text{Im}\left[\sum_j J_{AB,j} \exp(-i\mathbf{k} \cdot \mathbf{e}_j)\right],$$

$$B_{xz} = g \sin[\mathbf{k} \cdot (\mathbf{e}_0 - \mathbf{e}_2)] + g \sin[\mathbf{k} \cdot (\mathbf{e}_1 - \mathbf{e}_0)], \quad (5)$$

and $\mathbf{e}_0 = -a\hat{\mathbf{x}}$, $\mathbf{e}_1 = a(\hat{\mathbf{x}}/2 - \sqrt{3}/2\hat{\mathbf{y}})$, $\mathbf{e}_2 = a(\hat{\mathbf{x}}/2 + \sqrt{3}\hat{\mathbf{y}}/2)$. This model exhibits $\mathcal{P} = s_x\sigma_x$, $\mathcal{T} = is_yK$, and s_x symmetries. Utilizing the s_x symmetry, the Hamiltonian can be block diagonalized, and the SCN can be determined from the Chern number of one of these blocks. However, a limitation of this model is the inability to experimentally introduce additional terms to break the conserved spin symmetry or close the gap. This prevents the observation of a phase transition to topological insulator.

B. Model 2: A class

Because SCN can also be defined when TRS is broken [76], here we consider a construction of SCN without considering TRS. In this section, we can realize two Haldane models with opposite Chern numbers for different spins. We also consider additional terms that break spin conservation while maintaining the condition of not disrupting the double global degeneracy.

We start with cold fermions in a 2D setup, confined in a spin-dependent hexagonal optical lattice. This confinement is achieved by adjusting the light polarization between σ^+ and σ^-, as successfully demonstrated in experiments [78]. The hexagonal lattice can be regarded as a triangular lattice with a sublattice structure. In this arrangement, atoms occupy σ^+ and σ^- sites, experiencing a spin-dependent ac Stark shift within the light field. The overall potential is given by $V(\mathbf{r}) = V_{\text{hex}}(\mathbf{r}) + m_z V_{\text{tri}}(\mathbf{r})$. The fermion dynamics follow the Hamiltonian $H = \mathbf{p}^2/2m_0 + V(\mathbf{r})$.

The formation of a spin-dependent hexagonal optical lattice [78,79] is achieved through the intersection of three laser beams at a 120° angle, each linearly polarized in the x-y plane.

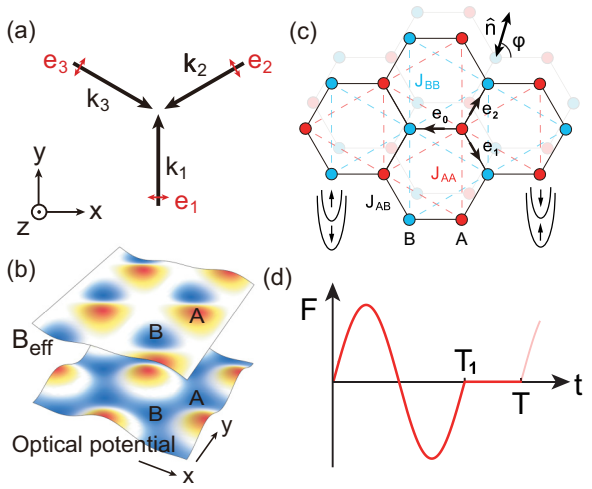

FIG. 2. (a) Laser setup of the two-dimensional hexagonal optical lattice. A spin-dependent sublattice potential Δ is introduced by controlling the local polarization. The trap's depth is not extremely strong, such that nNN hopping terms J_{AA} and J_{BB} cannot be ignored. (b) The strength of optical potential and effective magnetic field. (c) Tight-binding description of model. (d) Periodic modulation function.

The configuration of the three laser fields is as follows:

$$\begin{aligned}\mathcal{E}_1(\mathbf{r},t) &= E_0 e^{i(\mathbf{k}_1\cdot\mathbf{r}-\phi_1)-i\omega_L t}\mathbf{e}_x \\ \mathcal{E}_2(\mathbf{r},t) &= -E_0 e^{i(\mathbf{k}_2\cdot\mathbf{r}-\phi_2)-i\omega_L t}\left(\frac{1}{2}\mathbf{e}_x - \frac{\sqrt{3}}{2}\mathbf{e}_y\right) \\ \mathcal{E}_3(\mathbf{r},t) &= -E_0 e^{i(\mathbf{k}_3\cdot\mathbf{r}-\phi_3)-i\omega_L t}\left(\frac{1}{2}\mathbf{e}_x + \frac{\sqrt{3}}{2}\mathbf{e}_y\right).\end{aligned} \tag{6}$$

The spin-independent potential of 2D lattice $V_s = -\alpha_s|\mathcal{E}|^2$, given by $V_s(\mathbf{r}) = -\alpha_s E_0^2\{3-\cos(\mathbf{b}_1\cdot\mathbf{r})-\cos(\mathbf{b}_2\cdot\mathbf{r})-\cos[(\mathbf{b}_1-\mathbf{b}_2)\cdot\mathbf{r}]\}$ and $\mathbf{b}_1 = \mathbf{k}_2-\mathbf{k}_1$, $\mathbf{b}_2 = \mathbf{k}_3-\mathbf{k}_2$, $\mathbf{b}_3 = \mathbf{k}_1-\mathbf{k}_3$. The spin-dependent potential of 2D lattice $V_v = i\alpha_v(\mathcal{E}^*\times\mathcal{E})\cdot\mathbf{F}$, given by $V_v(\mathbf{r}) = \sqrt{3}\alpha_v E_0^2\mathbf{F}_z[\sin(\mathbf{b}_1\cdot\mathbf{r})+\sin(\mathbf{b}_2\cdot\mathbf{r})-\sin(\mathbf{b}_3\cdot\mathbf{r})]$ and shown in Fig. 2(b) as effective magnetic field $\mathbf{B}_{\text{eff}}$.

The tight-binding model, with a weak potential corresponding to the recoil energy E_R, enables the inclusion of a significant nNN term and can be expressed as

$$\begin{aligned}\hat{H}_{tb} = \sum_{\mathbf{r},\sigma} m_z\Delta(a^\dagger_{\mathbf{r},\sigma}a_{\mathbf{r},\sigma} - b^\dagger_{\mathbf{r},\sigma}b_{\mathbf{r},\sigma}) + \Bigg(\sum_{\mathbf{r},\mathbf{s}} J^{(\sigma)}_{AB}a^\dagger_{\mathbf{r},\sigma}b_{\mathbf{s},\sigma} \\ + \sum_{\langle\langle\mathbf{r},\mathbf{s}\rangle\rangle,\sigma} J^{(\sigma)}_{AA}a^\dagger_{\mathbf{r},\sigma}a_{\mathbf{s},\sigma} + J^{(\sigma)}_{BB}b^\dagger_{\mathbf{r},\sigma}b_{\mathbf{s},\sigma} + \text{H.c.}\Bigg).\end{aligned} \tag{7}$$

The tunneling amplitudes can be calculated from the overlap of the Wannier function. Since the potential for a spin-up atom at sublattice A is identical to a spin-down atom at sublattice B, the Wannier packet with different spins should satisfy $w_{\uparrow,A}(\mathbf{r}) = w_{\downarrow,B}(\mathbf{r})$ and $w_{\downarrow,A}(\mathbf{r}) = w_{\uparrow,B}(\mathbf{r})$. This property implies that the NN hopping is spin independent, and the nNN hopping satisfies $J^{\uparrow}_{AA} = J^{\downarrow}_{BB}$, $J^{\downarrow}_{AA} = J^{\uparrow}_{BB}$.

Here, we consider the periodic driving optical lattice shown in Fig. 2(c), described by the free fermion Hamiltonian

$$\hat{H}(t) = \hat{H}_{tb} + \sum_{\mathbf{r}} \boldsymbol{F}(t)\cdot\mathbf{r}(\hat{n}_{A,\mathbf{r}} + \hat{n}_{B,\mathbf{r}}). \tag{8}$$

The term $\hat{H}_{os}$ collects on-site terms describing many-body interactions or a weak static potential. In our model, the modulation involves moving the lattice along a periodic trajectory $\mathbf{r}(t)$, which introduces an inertial force $\boldsymbol{F}(t) = -m_0\ddot{\mathbf{r}}_{\text{lat}}(t)$ acting on the atoms. This additional time-dependent term can be canceled by a unitary transformation $U(t) = \exp[-im_0\sum_{\mathbf{r}}\dot{\mathbf{q}}_{\text{lat}}(t)\cdot\mathbf{r}(\hat{n}_{A,\mathbf{r}}+\hat{n}_{B,\mathbf{r}})]$, where $\mathbf{q}_{\text{lat}} = m_0[\dot{\mathbf{r}}_{\text{lat}}(t) - \dot{\mathbf{r}}_{\text{lat}}(0)]$ introduces a complex phase factor to the tunneling amplitudes. If there is no spin-flipping term, s_z is conserved and the Hamiltonian can be divided into two individual parts.

For a simple case in our Floquet gauge, if we only consider the zero-order term [80–82], the Floquet Hamiltonian is the time average $H_{\text{eff}} = \langle H(t)\rangle_T$ as long as the recoil energy E_R is significantly larger than both the nearest-neighbor hopping J and the energy scales of Hamiltonian. In this treatment, the effective tunneling after one period is given by

$$\left|J^{(\text{eff})}_{ij}\right|e^{i\theta_{ij}} = \langle J_{ij}e^{-i\mathbf{q}_{\text{lat}}\cdot\mathbf{r}_{ij}}\rangle_T. \tag{9}$$

Moreover, for sinusoidal forcing, such dynamics modification of tunneling is restricted to $\theta_{ij} = 0$ or π [83–86]. This phenomenon has been observed in several experiments [87–89]. The Peierls phase θ_{ij} also can be smoothly tuned to any value through appropriate driving [81,90]. Here, we consider a linear shaking scheme: the inertial force comprises a series of sinusoidal pulses separated by periods of rest with a periodicity of $T = T_1 + T_2$, as illustrated in Fig. 2(d).

$$\boldsymbol{F}(t) = \begin{cases} F_0\sin\omega_1(t \mod T)\hat{\mathbf{n}}, & 0 < (t \mod T) < T_1, \\ 0, & T_1 < (t \mod T) < T, \end{cases} \tag{10}$$

where $\omega_1 = 2\pi/T_1$ and the shaking axis is given by $\hat{\mathbf{n}} = (\cos\varphi\mathbf{e}_x + \sin\varphi\mathbf{e}_y)$. The effective hopping will be renormalized and multiplied by a phase factor

$$\langle e^{-i\mathbf{q}_{\text{lat}}\cdot\mathbf{r}_{ij}}\rangle_T = \frac{T_1}{T}e^{i\alpha_{ij}}\mathcal{J}_0(\alpha_{ij}) + \frac{T_2}{T}, \tag{11}$$

where $\alpha_{ij} = F_0\hat{\mathbf{n}}\cdot\mathbf{r}_{ij}/\omega_1$ and $\mathcal{J}_n$ represents n-order Bessel function. If $T_2 \neq 0$, the Peierls phase θ_{ij} is not a linear function of $\mathbf{r}_{ij}$, but

$$\tan\theta_{ij} = \frac{\sin\alpha_{ij}}{\cos\alpha_{ij} + \frac{T_2}{T_1\mathcal{J}_0(\alpha_{ij})}}, \tag{12}$$

and this gives rise to an inhomogeneous finite artificial magnetic flux through the elementary triangular plaquettes of 2D lattices. The effective Floquet Hamiltonian in momentum space can always be expressed as two distinct parts (details in Appendix B),

$$\hat{H}_{\text{eff}}(\mathbf{k}) = \lambda_+ I_4 + B_x(\mathbf{k})\sigma_x + B_y(\mathbf{k})\sigma_y + B_z(\mathbf{k})s_z\sigma_z, \tag{13}$$

and the ground state is always twofold degenerate. This model exhibits a topological phase transition when the gap closes, achieved by controlling the shaking amplitude F, shaking direction φ, and sublattice potential Δ. The phase diagram and

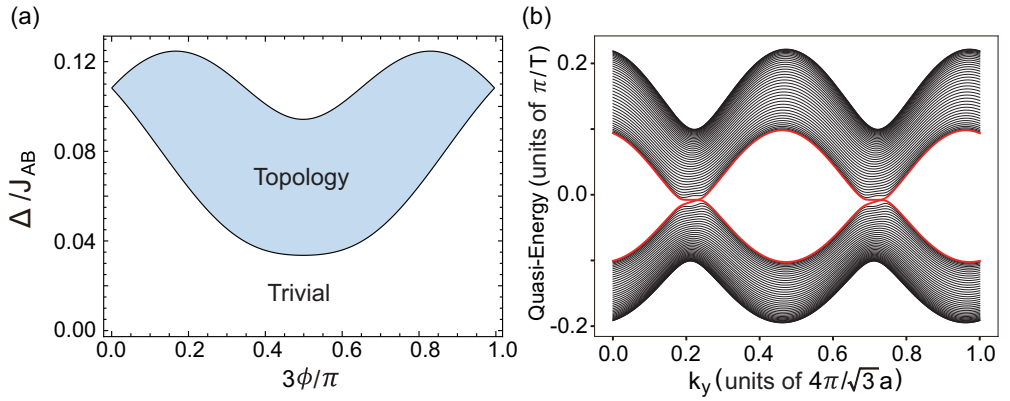

FIG. 3. (a) The phase diagram of the topological phase. (b) The corresponding Floquet band structure in topological phase with open boundary condition along the x direction. The calculated parameters include $J_{AA} = 0.1J_{AB}$, $J_{BB} = 0$, $T_1 = T/2$, $\omega/J_{AB} = 20$, and $F_0 a/\omega_1 \approx 1.89$. Additional parameters relevant to the experiment are provided in Sec. V.

Floquet bands are shown in Fig. 3, illustrating the possibilities for realizing a system with nontrivial topological invariants.

To break s_z symmetry but still keep the degeneracy of ground states, we consider adding some "flattened" terms [11] in Bloch Hamiltonian

$$H_{\mathrm{SF}}(\mathbf{k}) = g_R(\mathbf{k}) s_x \sigma_z + g_I(\mathbf{k}) s_y \sigma_z, \tag{14}$$

which represents all sublattice-dependent same-sublattice spin-flip processes. The σ_z term implies that coupling for different sublattices should take a π phase difference. To introduce terms like this and avoid the influence of periodic shaking, one method is to only consider on-site terms. However, there are no techniques to independently introduce local spin-flip terms in the Hamiltonian so far. As for building nNN Raman processes, it is difficult to control the hopping phase due to the effect of periodic shaking. Therefore, these terms cannot be realized in our Floquet system. However, one can always choose four internal states and carefully design and couple a system with Raman fields, as demonstrated in Ref. [91]. In that case, any possible coupling could be realized, and these terms can be realized.

To discuss SCN with the existence of these terms, the wave functions of the valence bands can be written as a tensor product: $|E_i(\mathbf{k})\rangle = |s_i(\mathbf{k})\rangle \otimes |\tau_i(\mathbf{k})\rangle$, where $|s_i\rangle$ and $|\tau_i\rangle$ represent wave functions for spin and sublattice, respectively. For the Hamiltonian given by Eq. (13) with the spin-flipping term, we can introduce two rotations along the σ_x and σ_y directions for each spin component simultaneously using $U_x = e^{-i\eta s_x/2} \otimes I_2$ and $U_y = e^{-i\xi s_y/2} \otimes I_2$. By performing the transformation $U_x^\dagger U_y^\dagger H U_y U_x = \mathcal{H}$, the spin-flipping term can be eliminated, with $\tan\xi = g_R/B_z$ and $\tan\eta = -g_I/\sqrt{B_z^2 + g_R^2}$ (the introduction of η is unnecessary when $g_I = 0$). The $s_z\sigma_z$ component of the block diagonalized Hamiltonian changes from B_z to $\widetilde{B}_z = -g_I \sin\eta + \cos\eta(B_z \cos\xi + g_R \sin\xi)$. The corresponding wave functions for spin and sublattice components are

$$\begin{aligned}
|s_1\rangle &= \left(\cos\frac{\eta}{2}\cos\frac{\xi}{2} + i\sin\frac{\eta}{2}\sin\frac{\xi}{2}\right)|\uparrow\rangle \\
&\quad + \left(\cos\frac{\eta}{2}\sin\frac{\xi}{2} - i\sin\frac{\eta}{2}\cos\frac{\xi}{2}\right)|\downarrow\rangle, \\
|s_2\rangle &= -\left(\cos\frac{\eta}{2}\sin\frac{\xi}{2} + i\sin\frac{\eta}{2}\cos\frac{\xi}{2}\right)|\uparrow\rangle \\
&\quad + \left(\cos\frac{\eta}{2}\cos\frac{\xi}{2} - i\sin\frac{\eta}{2}\sin\frac{\xi}{2}\right)|\downarrow\rangle, \\
|\tau_1\rangle &= \sin\frac{\theta}{2}|A\rangle - e^{i\varphi}\cos\frac{\theta}{2}|B\rangle, \\
|\tau_2\rangle &= e^{-i\varphi}\cos\frac{\theta}{2}|A\rangle - \sin\frac{\theta}{2}|B\rangle,
\end{aligned} \tag{15}$$

where $\tan\theta = \sqrt{B_x^2 + B_y^2}/\widetilde{B}_z$ and $\tan\varphi = B_y/B_x$. It should be noted that $\langle s_m|s_n\rangle = \delta_{mn}$ and $\langle\tau_m|\tau_n\rangle \neq \delta_{mn}$.

By introducing additional terms to break the $\hat{s}_z$ symmetry, we can follow the definition in Sec. II and express $\hat{P}\hat{s}_z\hat{P}$ to obtain a new reduced spin Hamiltonian denoted as $\mathscr{H}(\mathbf{k})$,

$$\mathscr{H}(\mathbf{k}) = \begin{pmatrix} M(\mathbf{k}) & t(\mathbf{k}) \\ t^*(\mathbf{k}) & -M(\mathbf{k}) \end{pmatrix}, \tag{16}$$

where $M(\mathbf{k}) = \langle E_{-,1}|\hat{s}_z|E_{-,1}\rangle = -\langle E_{-,2}|\hat{s}_z|E_{-,2}\rangle$ and $t(\mathbf{k}) = \langle E_{-,1}|\hat{s}_z|E_{-,2}\rangle$. These parameters can be represented by θ, ϕ, ξ, and η, with $M = \cos\eta\cos\xi$ and $t = -e^{-i\varphi}\sin\theta(\sin\xi + i\cos\xi\sin\eta)$. The gap of $\mathscr{H}$ will only close if both M and t are equal to 0, which corresponds to $\theta = 0$, $\xi = \eta = \pi/2$. The phase diagram takes the same form as the result shown in Fig. 3, and the magnitude of g_R and g_I do not relate to the phase transition. Up to this point, we can apply the same approach to calculate the SCN using the reduced spin Hamiltonian in such gapped models.

IV. DETECT METHOD IN COLD-ATOM SYSTEM

Cold-atom systems with optical lattices provide a clean platform for simulating and studying lattice models in condensed matter physics. Information about the interference pattern of Bloch states in this system can be extracted by measuring the ToF image. In general, the tomography method can provide complete information about the occupied bands. The tomography of a system with many bands is complicated. Therefore, we limit our consideration to a four-band model with twofold global degeneracy, which simplifies the tomography procedure. In cold-atom systems, various quench sequences can be employed to achieve tomography and

investigate Bloch states in optical lattices through the measurement of ToF images. In the preceding section, we give the method to realize tomography of twofold degeneracy space.

Firstly, we will outline the theory behind tomography measurements. In the absence of a Rashba SOC term that couples different spin components, information about each spin component can be independently extracted by measuring the ToF image and spin [11,49,50]. In a finite-size system, the density distribution of the ToF image with spin σ in momentum space can be calculated using

$$n_\sigma(\mathbf{k}) = f(\mathbf{k}) \sum_{m,n} e^{-i\mathbf{k}\cdot(\mathbf{r}_m-\mathbf{r}_n)} e^{i(\mu_{m,\sigma}-\mu_{n,\sigma})t} \times \langle G| [a^\dagger_{m,\sigma}, b^\dagger_{m,\sigma}] \begin{bmatrix} a_{n,\sigma} \\ b_{n,\sigma} \end{bmatrix} |G\rangle , \tag{17}$$

where $f(\mathbf{k})$ represents a broad envelope function determined by the momentum distribution of the Wannier function, and $\mu_{n,\sigma}$ denotes the global trap potential strength at site i. In the absence of a global trapping difference, one has $\mu_{n,\sigma} = \mu_s$.

The density distribution of the ToF image is given by $n_\sigma(\mathbf{k}) = f(\mathbf{k}) \langle G| \sigma_0 + \sigma_x |G\rangle$, where $|G\rangle$ represents the many-particle states with Fermi energy E_f in an ideal periodic system without trapping differences. A quench involving the Pauli matrix σ_z generates the evolution operator $\exp(-i\sigma_z t/2)$, which transforms the ToF image from σ_x to $\sigma_x \cos t - \sigma_y \sin t$. By choosing $t = 0$ and $t = \pi/2$, the expectation values $\langle\sigma_x\rangle$ and $\langle\sigma_y\rangle$ can be extracted. Extracting $\langle\sigma_z\rangle$ can follow a similar approach to that used for the σ_y quench. However, in the case of isolated band tomography, one σ_z quench is sufficient to recover σ_z by analyzing the evolution curve of quench dynamics [49,50].

For the four-band model with degeneracy, it is necessary to measure all five components of the Dirac matrices from tomography. In the case of a finite-size system, the overall density distribution of the ToF image in momentum space can be calculated using

$$n(\mathbf{k}) = f(\mathbf{k}) \sum_{m,n} e^{-i\mathbf{k}\cdot(\mathbf{r}_m-\mathbf{r}_n)} e^{i(\mu_{m,\sigma}-\mu_{n,\sigma})t} \times \langle G| C^\dagger_n C_m |G\rangle , \tag{18}$$

where $C_j = [a_{j,\uparrow}, b_{j,\uparrow}, a_{j,\downarrow}, b_{j,\downarrow}]^T$. For an ideal periodic system without trapping differences, the density distribution of the ToF image in Eq. (18) can be expressed by $n(\mathbf{k}) = f(\mathbf{k}) \langle G| \Gamma_0 + \Gamma_1 - \Gamma_{23} + \Gamma_{45} |G\rangle$. For example, since the system in the above section only has Γ_1, Γ_{12}, Γ_{13}, Γ_{14}, and Γ_{15} components, the expectation value of other components should be zero. In this context, we consider a simplified case where $\eta = 0$ or $g_I = 0$. Three possible quench sequences can simplify the tomography of such a system in an optical lattice: Γ_2, Γ_{12}, and Γ_{14} (Appendix F). The parameters θ, ϕ, and ξ can all be extracted from the ToF images obtained with these different quench sequences.

For the first model generated by Raman lattice, the topological invariants could be extracted directly by measuring the ToF image of each spin part. For the second model, additional terms gap the system, but we could still reconstruct the spin Hamiltonian using these parameters from tomography and get a nontrivial SCN.

The SCN can be expressed as momentum-space integrals of the spin Berry curvature $F^{(s)}_{xy}(\mathbf{k}) = \partial_{k_x} A^{(s)}_y(\mathbf{k}) - \partial_{k_y} A^{(s)}_x(\mathbf{k})$ and connection $A^{(s)}_\mu(\mathbf{k}) = i \langle u_s(\mathbf{k})| \partial_{k_\mu} |u_s(\mathbf{k})\rangle$ associated with the Bloch state $|u_s(\mathbf{k})\rangle$. The integration is over the whole BZ, forming a compact manifold. If the gauge potential $A^{(s)}_\mu(\mathbf{k})$ is globally well defined over the BZ, the SCN vanishes because the torus has no boundary. If some topological obstacle exists, the curvature can be solved by Fukui's $U(1)$ link method [92]: $U_\mu(\mathbf{k}) = \langle u(\mathbf{k})|u(\mathbf{k}+\delta\mathbf{k}_\mu)\rangle / |\langle u(\mathbf{k})|u(\mathbf{k}+\delta\mathbf{k}_\mu)\rangle|$ and $\mathcal{F}_{\mu\nu}(\mathbf{k}) = i \ln[U_\mu(\mathbf{k}) U_\nu(\mathbf{k}+\delta\mathbf{k}_\mu) U^{-1}_\nu(\mathbf{k}) U^{-1}_\mu(\mathbf{k}+\delta\mathbf{k}_\nu)]$, where $\mathcal{F}_{\mu\nu}(\mathbf{k}) \in (-\pi, \pi]$ as a discrete version. It can be obtained from the ToF image evolution associated with the pixel $\mathbf{k}$. The topological invariants of the reduced spin Hamiltonian $\mathcal{H}$ can be calculated from $\mathcal{F}^{(s)}_{\mu\nu}(\mathbf{k})$ by directly summing over all pixels of the BZ.

To demonstrate the efficiency of the tomography method, we utilize a finite-size system to compute its ToF images. For a quadratic Hamiltonian in real space that is characterized by free fermions, the Hamiltonian is given by

$$H = \sum_{\mathbf{r},\mathbf{s},\alpha,\beta} (a^\dagger_{\mathbf{s},\beta}, b^\dagger_{\mathbf{s},\beta}) \mathcal{H}_{\mathbf{r}\alpha,\mathbf{s}\beta} \begin{pmatrix} a_{\mathbf{r},\alpha} \\ b_{\mathbf{r},\alpha} \end{pmatrix}, \tag{19}$$

where $\mathbf{r}$ and $\mathbf{s}$ represent position indices, and α and β represent spin indices. A unitary operation exists to diagonalize this Hamiltonian, resulting in $\mathcal{H} = U^\dagger \Lambda U$. The unitary transformation and the diagonalized Hamiltonian can be expressed as follows:

$$\begin{aligned} c_{\mathbf{q},\delta} &= \sum_{\mathbf{s},\beta} U^{(a\to c)}_{\mathbf{q}\delta,\mathbf{s}\beta} a_{\mathbf{s},\beta} + U^{(b\to c)}_{\mathbf{q}\delta,\mathbf{s}\beta} b_{\mathbf{s},\beta}, \\ d_{\mathbf{q},\delta} &= \sum_{\mathbf{s},\beta} U^{(a\to d)}_{\mathbf{q}\delta,\mathbf{s}\beta} a_{\mathbf{s},\beta} + U^{(b\to d)}_{\mathbf{q}\delta,\mathbf{s}\beta} b_{\mathbf{s},\beta}, \end{aligned} \tag{20}$$

and

$$H = \sum_{\mathbf{q},\delta} \Lambda^{(c)}_{\mathbf{q},\delta} c^\dagger_{\mathbf{q},\delta} c_{\mathbf{q},\delta} + \Lambda^{(d)}_{\mathbf{q},\delta} d^\dagger_{\mathbf{q},\delta} d_{\mathbf{q},\delta}, \tag{21}$$

where the quasi-particles $c_{\mathbf{q},\delta}$ and $d_{\mathbf{q},\delta}$ correspond to lower and higher energy levels, respectively, with δ representing the pseudospin index. The particle number $\mathcal{N}$ is conserved and defined as $\mathcal{N} = \sum_{\mathbf{r},\alpha} (a^\dagger_{\mathbf{r},\alpha} a_{\mathbf{r},\alpha} + b^\dagger_{\mathbf{r},\alpha} b_{\mathbf{r},\alpha})$. In such a system, particles occupy the top $\mathcal{N}$ eigenmodes with the lowest eigenenergy at absolute zero temperature. Consequently, by manipulating the Fermi energy E_F of this system—effectively controlling $\mathcal{N}$—the system's ground state can be described as $|G\rangle = \prod_{j=1}^{\mathcal{N}_d} d^\dagger_j \prod_{i=1}^{\mathcal{N}_c} c^\dagger_i |0\rangle$, where indices i and j are arranged based on the energy of the quasi-particles $c_{\mathbf{q},\delta}$ and $d_{\mathbf{q},\delta}$. By substituting the terms $a_{\mathbf{r},\sigma}$ and $b_{\mathbf{r},\sigma}$ into Eq. (18), the momentum density distribution of a finite-size system can be computed (Appendix D).

Here, we present the numerical simulations of the model we constructed in Eq. (13), augmented with terms Eq. (14) as a constant. Despite the complex parameters generated by periodic shaking, we focus solely on the model described in Eq. (13) with a simplified parameter configuration. Specifically, the nNN hopping is spatially uniform and set at $0.1J_{\mathrm{NN}}$ with a phase of $\pm\pi/2$ from different spin components. We consider a finite lattice with dimensions $8 \times 8 \times 2$ sites,

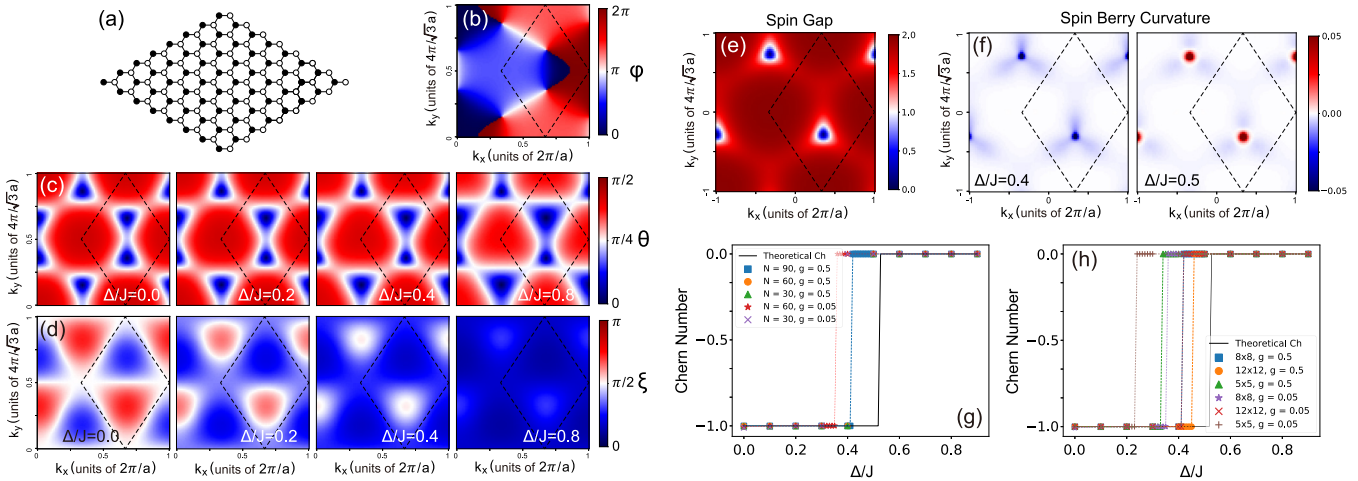

FIG. 4. (a) Calculations are performed on a honeycomb lattice with $N = 8 \times 8 \times 2$ sites and two spin degrees of freedom. Parameters are extracted from the ToF image: (b) φ, (c) θ, and (d) ξ. The black dashed line represents the boundary of BZ. (e) Spin gap near the phase transition point. (f) Spin Berry curvature of the topological and trivial phases. (g) Extracted spin Chern number vs different resolution ratios with a strong or weak g term. (h) Extracted spin Chern number vs different lattice sizes with a strong or weak g term. The calculated parameters are as follows: $J^{\pm}_{\mathrm{nNN}} = \pm 0.1iJ_{\mathrm{NN}}$, $J_{BB} = 0$, and $g = 0.5J_{\mathrm{NN}}$.

investigate quench dynamics and obtained results displayed in Fig. 4. The reconstructed spin Hamiltonian exhibits a gapless point if and only if $\theta = 0$ and $\xi = \pi/2$. Analyzing the data in Fig. 4(c), we observe that θ consistently features two zero points across the entire BZ. On the other hand, for the parameter ξ, as Δ increases, the $\xi = \pi/2$ regions contract to discrete points. Remarkably, these points also adhere to $\theta = 0$, establishing them as gapless points in the reduced spin Hamiltonian. Consequently, we can find a change in the SCN through calculations of spin-Berry curvature.

The extracted spin gap and spin Berry curvature are illustrated in Figs. 4(e) and 4(f). Within the BZ, a single gapless point is observed, and the spin Berry curvature exhibits significant numerical values around these gapless points in Fig. 4(f). When evaluating the SCN with different resolution ratios and strengths of the g term, it is remarkable that the simulated SCN remains nearly unaffected by the resolution ratio of the ToF image in Fig. 4(g). However, the strength of the g term does influence the location of the phase transition point. Notably, the phase transition point $\Delta = \pm 3\sqrt{3}J_{\mathrm{nNN}}$ remains entirely independent of the parameter g, implying that the observed deviations can be viewed as amplification of the effect on system size.

Considering both a strong and weak g term, a comparison of the simulated SCNs across various lattice sizes is presented in Fig. 4(h). With the increasing of system size, the phase transition point approaches the theoretical point. For the effect of g, across most regions except for the vicinity of $B_z = 0$, ξ predominantly assumes values close to either 0 or π. In scenarios involving a weak g term, changes in ξ tend to be abrupt, leading to the need for more and more precise samplings. Consequently, determination of the accurate phase transition point becomes challenging, resulting in a notable discrepancy between numerical and theoretical outcomes, as evident in Fig. 4(h).

V. DISCUSSION AND CONCLUSION

In order to establish a connection with experiments involving cold atoms, we consider ^{6}Li atoms with parameters as reported in Refs. [45,53]. For the lattice configuration, we set the depths to approximately $J_{AB}/2\pi = 5$ kHz, $J_{AA}/2\pi = 500$ Hz, and $J_{BB}/2\pi \ll J_{AA}$. The lattice constant is determined by the wavelength $\lambda = 1064$ nm of the laser beams used to create the optical lattice. The sinusoidal modulation of the lattice position along the x and y directions is characterized by a shaking amplitude of 0.1λ. To capture the dynamics, the modulation frequency $\omega_1/2\pi$ can be configured to exceed 100 kHz.

In experimental setups, several parameters can introduce perturbations to the ToF image. However, the trapping frequencies of the global weak underlying harmonic confinement are notably smaller than J_{AB} and can thus be safely disregarded within theoretical discussions. In Fig. 3, observing the nontrivial topological phase requires a Δ range of approximately $0.06J_{AB}$ using feasible experimental parameters. Correspondingly, this frequency value corresponds to around 300 Hz. The main factor that affects the energy gap is the g term that destroys spin conservation. As a result of the gap increasing, the occupations in the conducting band are also suppressed. Therefore, a larger g can effectively suppress thermal fluctuations. Therefore, a larger g can effectively suppress thermal fluctuations.

The introduction of a spin-dependent nNN hopping term can be achieved through a global spin-dependent potential. Meanwhile, the creation of opposing artificial magnetic fluxes for each spin component can be realized via optical potential modulation. This artificial magnetic field primarily originates from the zero-order contribution of the intrinsic nNN hopping term and proves easy to prepare and detect, particularly in systems characterized by shallow potentials.

Furthermore, the broader extended Wannier function that we propose here serves a dual purpose: it not only enhances the nNN hopping amplitude but also amplifies the strength of many-body interactions. This amplification can introduce non-negligible effects stemming from many-body terms. However, the impact of these many-body interactions can be mitigated by manipulating the scattering length of atoms through Feshbach resonance.

Additionally, the extension of our work opens avenues to explore topological phase transitions and other lattice model properties by extracting ToF images in future research endeavors. It is worth noting that all the parameters discussed here are actually independent. Altering the sublattice potential Δ simultaneously affects both NN and nNN hopping, rendering the actual phase diagram more intricate than what is depicted in Fig. 3. Importantly, all these parameters are tunable via adjustments to the optical potential.

VI. SUMMARY

We introduce achievable simple models demonstrating nontrivial SCN in ultracold-atom systems. We derive the spin-Hamiltonian and SCNs by analyzing essential parameters extracted from the quench dynamics of ToF images. It is crucial to highlight that in the topological phase, the orientation of currents in different spin sectors becomes variable, leading to quantized spin Hall currents. Moreover, the same quenching approach can be applied to topological insulators in alternative classes or systems with second-order topology, as long as it can be realized in an ultracold-atom system.

In summary, we systematically build two distinct four-band models with nontrivial topological invariants. These models enable measurable SCN in cold-atom experiments, and we propose a method to effectively probe their corresponding topological invariants. The strategies and examples provided in this study offer a foundation for realizing and detecting topological states in cold-atom systems. Additionally, these insights contribute to a deeper understanding of topological excitations and the broader concept of topological order, spanning various fields like condensed-matter physics and artificial systems.

ACKNOWLEDGMENTS

We thank Y. Q. Zhu, P. He, Z. Zheng, and S. L. Zhu for helpful discussions. This work was supported by the National Natural Science Foundation of China (Grant No. 12074180).

APPENDIX A: CONDITIONS OF FOUR-BAND MODEL WITH DEGENERACY

Firstly, we discuss the conditions when the four-band Hamiltonian shows degeneracy. An arbitrary four-band model can be represented by 15 Clifford matrices, where Clifford matrices are defined as $\Gamma_{(1,2,3,4,5)} = (I \otimes \sigma_x, I \otimes \sigma_z, s_x \otimes \sigma_y, s_y \otimes \sigma_y, s_z \otimes \sigma_y)$, and their ten commutators are $\Gamma_{ij} = [\Gamma_i, \Gamma_j]/(2i)$. If there exists global degeneracy, the Hamiltonian satisfies $H^2 \propto I$. Suppose $H = \sum_\mu g_\mu \Gamma_\mu + \sum_{\mu<\nu} g_{\mu\nu}\Gamma_{\mu\nu}$ and its square is

$$H^2 = \left(\sum_\mu g_\mu^2 + \sum_{\mu<\nu} g_{\mu\nu}^2\right) I_4 + \sum_{\mu<\nu} g_\mu g_\nu \{\Gamma_\mu, \Gamma_\nu\} + \sum_{\mu,\nu<\rho} g_\mu g_{\nu\rho}\{\Gamma_\mu, \Gamma_{\nu\rho}\} + \sum_{\mu<\nu,\rho<\lambda} g_{\mu\nu} g_{\rho\lambda}\{\Gamma_{\mu\nu}, \Gamma_{\rho\lambda}\},$$

and this implies all anticommutators are zero. Firstly, $\{\Gamma_\mu, \Gamma_\nu\} = 2\delta_{\mu\nu}$. For the last two terms with $\Gamma_{\mu\nu}$, $\{\Gamma_\mu, \Gamma_{\nu\rho}\} = 0$ if and only if $\mu = \nu$ or $\mu = \rho$. Similarly, if one index in $\{\mu, \nu\}$ is equal to $\{\rho, \lambda\}$, $\{\Gamma_{\mu\nu}, \Gamma_{\rho\lambda}\}$ also takes zero. Above all, we get two types of twofold global degenerate cases:

$$\begin{aligned} H_\mu &= \sum_\mu g_\mu \Gamma_\mu, \\ H_\mu &= g_\mu \Gamma_\mu + \sum_\nu g_\nu \Gamma_{\mu\nu}, \end{aligned} \tag{A1}$$

and these two types of Hamiltonians are equivalent by performing one unitary transformation. We could also observe that one four-band model with global degeneracy can have at most five different Clifford matrices.

APPENDIX B: EFFECTIVE FLOQUET HAMILTONIAN

Here, we explore the scenario of an optical lattice described by a tight-binding model, where each site accommodates one orbital. Additionally, an external gradient field is introduced,

$$H = \sum_{m,n} \left[\left(C_{m,n}^\dagger h C_{m,n} + C_{m+1,n}^\dagger T_{\mathbf{e}_1} C_{m,n} + C_{m,n+1}^\dagger T_{\mathbf{e}_2} C_{m,n} + \text{H.c.} \right) + C_{m,n}^\dagger \boldsymbol{F}(t) \cdot \mathbf{r} C_{m,n} \right],$$

where $C_{m,n} = [a_{m,n}, b_{m,n}]^T$. In our experiments, the modulation consists of displacing the lattice along a periodic trajectory denoted as $\mathbf{r}(t)$. This displacement introduces an inertial force $\boldsymbol{F}(t) = -m_0 \ddot{\mathbf{r}}_{\text{lat}}(t)$ acting on the atoms. To handle this additional time-dependent term, a unitary transformation can be applied to cancel it out:

$$\begin{aligned} U(t) &= \exp\left[-i m_0 \sum_{m,n} C_{m,n}^\dagger \int_0^t dt \ddot{\mathbf{r}}_{\text{lat}}(t) \cdot \mathbf{r} C_{m,n} \right] \\ &= \exp\left[-i m_0 \sum_{m,n} C_{m,n}^\dagger [\dot{\mathbf{r}}_{\text{lat}}(t) - \dot{\mathbf{r}}_{\text{lat}}(0)] \cdot \mathbf{r} C_{m,n} \right]. \end{aligned}$$

The modulation needs to satisfy the following condition: it must assume zero values at both the beginning and end of a period. To facilitate our treatment, we introduce the quantity $\mathbf{q}_{\text{lat}} = m_0[\dot{\mathbf{r}}_{\text{lat}}(t) - \dot{\mathbf{r}}_{\text{lat}}(0)]$. This formulation ensures that the gauge transformation adheres to the condition $U(0) = I$. In this case, all hopping terms will attach a phase factor $\exp[-i\mathbf{q}_{\text{lat}} \cdot (\mathbf{r}_{mn} - \mathbf{r}_{kl})]$. The effective Floquet Hamiltonian

in zero and first order are

$$H_F^{(0)}(t_0) = \frac{1}{T}\int_{t_0}^{t_0+T} dt H(t)$$
$$H_F^{(1)}(t_0) = \frac{1}{T}\frac{1}{2!i}\int_{t_0}^{t_0+T} dt_1 \int_{t_0}^{t_1} dt_2 [H(t_1), H(t_2)].$$

Following the calculations outlined in the main text, the effective hopping terms undergo renormalization, obtaining a phase factor denoted as θ_{ij} in Eq. (9). The resulting Floquet Bloch Hamiltonian can be conceptually regarded as a composite of two distinct and independent components. For the spin-up part, $B_x + iB_y = \frac{J_{AB}}{T}\sum_n [T_1 \mathcal{J}_0(\alpha_n) e^{-i(\mathbf{k}\cdot\mathbf{e}_n+\alpha_n)} + T_2 e^{-i\mathbf{k}\cdot\mathbf{e}_n}]$ and

$$B_z = \Delta + \underbrace{\frac{J_{AA}-J_{BB}}{T}\sum_{n=0}^{2}\sum_m \delta_{m,(n+1 \bmod 3)}\{T_1\mathcal{J}_0(\beta_n)\cos[\mathbf{k}\cdot(\mathbf{e}_n-\mathbf{e}_m)+\beta_n] + T_2\cos\mathbf{k}\cdot(\mathbf{e}_n-\mathbf{e}_m)\}}_{\lambda_-},$$

where $\alpha_n = F_0\hat{\mathbf{n}}\cdot\mathbf{e}_n/\omega_1$, $\beta_i = F_0\hat{\mathbf{n}}\cdot(\mathbf{e}_n - \mathbf{e}_{(n+1)\bmod 3})/\omega_1$ and $\mathbf{e}_0 = -a\hat{\mathbf{x}}$, $\mathbf{e}_1 = \frac{a}{2}\hat{\mathbf{x}} - \frac{\sqrt{3}a}{2}\hat{\mathbf{y}}$, $\mathbf{e}_2 = \frac{a}{2}\hat{\mathbf{x}} + \frac{\sqrt{3}a}{2}\hat{\mathbf{y}}$. The difference between the spin-up and spin-down part is the value of nNN hopping: $J_{AA}^{\uparrow} - J_{BB}^{\uparrow} = J_{BB}^{\downarrow} - J_{AA}^{\downarrow}$. This gives rise to Hamiltonian

$$H = \begin{pmatrix} \lambda_+\mathbf{I} + \boldsymbol{d}_+\cdot\boldsymbol{\sigma} & 0 \\ 0 & \lambda_+\mathbf{I} + \mathbf{d}_-\cdot\boldsymbol{\sigma}\end{pmatrix}, \tag{B2}$$

where $\mathbf{d}_\pm = [B_x, B_y, \pm(\Delta+\lambda_-)]$.

APPENDIX C: FLOQUET APPROXIMATION

We have formulated an effective Floquet model as discussed earlier. However, our analysis is confined to the zero-order Floquet approximation. We extend our examination to the effective Floquet Hamiltonian for first order following the approach outlined in Ref. [93]. Generally speaking, a Floquet gauge which has centrosymmetry can lead to an exact zero first term. However, there is no centrosymmetry in such a driving sequence even if the Floquet gauge is changed. By computing the maximum first-order term, we can identify the parameter conditions that validate the zero-order approximation. It is noteworthy that the term J_{AB}^2 significantly influences the diagonal elements and serves as the primary contributor to the maximum first-order Floquet Hamiltonian. The magnitude of the maximum first-order term can be expressed as follows:

$$\begin{aligned}\text{First order} &= J_{AB}^2\frac{1}{T}\frac{1}{2!i}\int_0^T dt_1 \exp[-i\mathbf{q}_{\text{lat}}(t_1)\cdot\mathbf{e}_n] \\ &\quad\times\int_0^{t_1} dt_2 \exp[i\mathbf{q}_{\text{lat}}(t_2)\cdot\mathbf{e}_m] \\ &\leqslant J_{AB}^2\frac{1}{T}\frac{1}{2!i}\left[\frac{T_1^2}{2} + T_1(T-T_1) + \frac{1}{2}(T-T_1)^2\right] \\ &= \frac{\pi J_{AB}^2}{2\omega},\end{aligned}$$

where all Bessel function $\mathcal{J}_n(z) \leqslant 1$ and driving frequency ω_1 should be sufficiently large to satisfy $\mathcal{J}_0(z) \gg \mathcal{J}_n(z)/\omega_1$. Actually, due to the contribution of $\mathcal{J}_0(\alpha_i)$ and the phase α_i, the norm of the first-order term is even smaller than $\pi J_{AB}^2/2\omega$. Notably, the diagonal term is chiefly influenced by $|J_{AA} - J_{BB}|$, which in our consideration is $0.1J_{AB}$. Consequently, this ensures that $|J_{AA} - J_{AB}| > \max\{\text{first order}\}$.

APPENDIX D: TIME-OF-FLIGHT INTERFERENCE IMAGE CALCULATION

The correlation function in real space can be calculated by

$$\begin{aligned}
\langle G|\, a_{\mathbf{r},\sigma}^\dagger a_{\mathbf{r}',\sigma}\,|G\rangle &= \sum_{\mathbf{s},\beta,\mathbf{s}',\beta'} U_{\mathbf{s}\beta,\mathbf{r}\sigma}^{(a\to c)}\left(U_{\mathbf{s}'\beta',\mathbf{r}'\sigma}^{(a\to c)}\right)^*\langle G|\, c_{\mathbf{s},\beta}^\dagger c_{\mathbf{s}',\beta'}\,|G\rangle + U_{\mathbf{s}\beta,\mathbf{r}\alpha}^{(a\to d)}\left(U_{\mathbf{s}'\beta',\mathbf{r}'\alpha'}^{(a\to d)}\right)^*\langle G|\, d_{\mathbf{s},\beta}^\dagger d_{\mathbf{s}',\beta'}\,|G\rangle \\
\langle G|\, b_{\mathbf{r},\sigma}^\dagger b_{\mathbf{r}',\sigma}\,|G\rangle &= \sum_{\mathbf{s},\beta,\mathbf{s}',\beta'} U_{\mathbf{s}\beta,\mathbf{r}\sigma}^{(b\to c)}\left(U_{\mathbf{s}'\beta',\mathbf{r}'\sigma}^{(b\to c)}\right)^*\langle G|\, c_{\mathbf{s},\beta}^\dagger c_{\mathbf{s}',\beta'}\,|G\rangle + U_{\mathbf{s}\beta,\mathbf{r}\sigma}^{(b\to d)}\left(U_{\mathbf{s}'\beta',\mathbf{r}'\sigma}^{(b\to d)}\right)^*\langle G|\, d_{\mathbf{s},\beta}^\dagger d_{\mathbf{s}',\beta'}\,|G\rangle \\
\langle G|\, a_{\mathbf{r},\sigma}^\dagger b_{\mathbf{r}',\sigma}\,|G\rangle &= \sum_{\mathbf{s},\beta,\mathbf{s}',\beta'} U_{\mathbf{s}\beta,\mathbf{r}\sigma}^{(a\to c)}\left(U_{\mathbf{s}'\beta',\mathbf{r}'\sigma}^{(b\to c)}\right)^*\langle G|\, c_{\mathbf{s},\beta}^\dagger c_{\mathbf{s}',\beta'}\,|G\rangle + U_{\mathbf{s}\beta,\mathbf{r}\sigma}^{(a\to d)}\left(U_{\mathbf{s}'\beta',\mathbf{r}'\sigma}^{(b\to d)}\right)^*\langle G|\, d_{\mathbf{s},\beta}^\dagger d_{\mathbf{s}',\beta'}\,|G\rangle \\
\langle G|\, b_{\mathbf{r},\sigma}^\dagger a_{\mathbf{r}',\sigma}\,|G\rangle &= (\langle G|\, a_{\mathbf{r},\sigma}^\dagger b_{\mathbf{r}',\sigma}\,|G\rangle)^*,
\end{aligned} \tag{D1}$$

and in real space, ground state $|G\rangle$ satisfies

$$\langle G|\, c_{\mathbf{s},\beta}^\dagger c_{\mathbf{s}',\beta'}\,|G\rangle = \langle G|\, d_{\mathbf{s},\beta}^\dagger d_{\mathbf{s}',\beta'}\,|G\rangle = \delta_{\mathbf{s},\mathbf{s}'}\delta_{\beta,\beta'}\theta(E_F - \mathcal{E})$$
$$\langle G|\, c_{\mathbf{s},\beta}^\dagger d_{\mathbf{s}',\beta'}\,|G\rangle = \langle G|\, d_{\mathbf{s},\beta}^\dagger c_{\mathbf{s}',\beta'}\,|G\rangle = 0,$$

where $\theta(E_F - \mathcal{E})$ is the Heaviside function which describes the Fermi-Dirac distribution at zero temperature. Thus, the momentum density of a finite-size model can be calculated by

$$\langle G|\, a_{\mathbf{r},\alpha}^\dagger a_{\mathbf{r}',\alpha'}\,|G\rangle = \sum_{\mathbf{s},\beta} U_{\mathbf{s}\beta,\mathbf{r}\sigma}^{(a\to c)}\left(U_{\mathbf{s}\beta,\mathbf{r}'\sigma}^{(a\to c)}\right)^*$$
$$\langle G|\, b_{\mathbf{r},\alpha}^\dagger b_{\mathbf{r}',\alpha'}\,|G\rangle = \sum_{\mathbf{s},\beta} U_{\mathbf{s}\beta,\mathbf{r}\sigma}^{(b\to c)}\left(U_{\mathbf{s}\beta,\mathbf{r}'\sigma}^{(b\to d)}\right)^*$$

$$\langle G|\, a^{\dagger}_{\mathbf{r},\sigma} b_{\mathbf{r}',\sigma}\, |G\rangle = \sum_{\mathbf{s},\beta} U^{(a\to c)}_{\mathbf{s}\beta,\mathbf{r}\sigma} \left(U^{(b\to c)}_{\mathbf{s}\beta,\mathbf{r}'\sigma}\right)^*$$

$$\langle G|\, b^{\dagger}_{\mathbf{r},\sigma} a_{\mathbf{r}',\sigma}\, |G\rangle = \left(\langle G|\, a^{\dagger}_{\mathbf{r}',\sigma} b_{\mathbf{r},\sigma}\, |G\rangle\right)^*. \tag{D2}$$

APPENDIX E: TOMOGRAPHY PROCEDURE

In the context of the twofold globally degenerate system described by Eqs. (13) and (14), and considering the ground state as $|G\rangle = (\prod_{\mathbf{k}\in \mathrm{BZ}} c^{\dagger}_{-,2})(\prod_{\mathbf{k}\in \mathrm{BZ}} c^{\dagger}_{-,1})\,|0\rangle$, it suffices to measure $\langle\Gamma_1\rangle$, $\langle\Gamma_{12}\rangle$, $\langle\Gamma_{13}\rangle$, and $\langle\Gamma_{15}\rangle$ in order to complete the entire tomography process. The theoretical values for the ToF image under periodic boundary conditions are as follows:

$$\langle\Gamma_1\rangle = -2\cos\varphi\sin\theta, \quad \langle\Gamma_{12}\rangle = -2\sin\varphi\sin\theta$$
$$\langle\Gamma_{13}\rangle = -2\sin\xi\cos\theta, \quad \langle\Gamma_{15}\rangle = -2\cos\xi\cos\theta. \tag{E1}$$

It is important to note that all other components of the Gamma matrices are zero. The total density distribution of the ToF image in momentum space can be calculated by

$$\begin{aligned} n(\mathbf{k}) &= f(\mathbf{k})\,\langle\Gamma_0 + \Gamma_1 - \Gamma_{23} + \Gamma_{45}\rangle \\ &= f(\mathbf{k})(2 - 2\cos\varphi\sin\theta). \end{aligned} \tag{E2}$$

Here, we contemplate a quench that transforms the initial ground state $|G\rangle$ into a new state $|\widetilde{G}\rangle = \exp(-i\Gamma t/2)\,|G\rangle$. In the absence of a quench, we have $n(k) = \langle\Gamma_0\rangle + \langle\Gamma_1\rangle$. Considering all possible quench scenarios that can provide relevant information, we present them as follows:

$$\begin{aligned} \Gamma_2 &: n(\mathbf{k},t) = \langle\Gamma_0\rangle + \cos t\,\langle\Gamma_1\rangle + \sin t\,\langle\Gamma_{12}\rangle \\ \Gamma_3 &: n(\mathbf{k},t) = \langle\Gamma_0\rangle + \cos t\,\langle\Gamma_1\rangle + \sin t\,\langle\Gamma_{13}\rangle \\ \Gamma_5 &: n(\mathbf{k},t) = \langle\Gamma_0\rangle + \cos t\,\langle\Gamma_1\rangle + \sin t\,\langle\Gamma_{15}\rangle \\ \Gamma_{12} &: n(\mathbf{k},t) = \langle\Gamma_0\rangle + \cos t\,\langle\Gamma_1\rangle - \sin t\,\langle\Gamma_{13}\rangle \\ \Gamma_{13} &: n(\mathbf{k},t) = \langle\Gamma_0\rangle + \cos t\,\langle\Gamma_1\rangle + \sin t\,\langle\Gamma_{12}\rangle \\ \Gamma_{14} &: n(\mathbf{k},t) = \langle\Gamma_0\rangle + \cos t\,\langle\Gamma_1\rangle + \sin t\,\langle\Gamma_{15}\rangle\,. \end{aligned} \tag{E3}$$

By setting $t = 0, \pi/2, \pi$, all components can be exacted from

$$\frac{n(\pi/2)}{n(0)+n(\pi)} = \frac{\langle\Gamma_0\rangle + \langle\Gamma\rangle}{2\,\langle\Gamma_0\rangle} = \frac{1}{2}\left(1 + \frac{\langle\Gamma\rangle}{\langle\Gamma_0\rangle}\right). \tag{E4}$$

The contribution of the broad envelope can be evaluated as background by calculating the sum at $t = 0$ and $t = \pi$.

APPENDIX F: EXPERIMENTAL SETUP OF OPTICAL LATTICE AND QUENCH DYNAMICS

In order to realize different types of quench smoothly, the optical lattice can be formed by stacked hexagonal optical potential. To achieve a Γ_2-type quench, one part is formed by the setting in model 2 in Sec. IV, and another part can be achieved by three detuned standing-wave laser fields that are rotated by angles of $\pi/3$ with respect to each other:

$$\mathcal{E}_j(\mathbf{r},t) = E_0 e^{-i\omega' t}\sin(\mathbf{k}'_i\cdot\mathbf{r} + \phi_i)\mathbf{e}_z \tag{F1}$$

and $V_s(\mathbf{r}) = -\alpha_s|\sum_{j=1}^{3}\mathcal{E}_j(\mathbf{r})|^2$. By appropriately selecting values for the phases ϕ_i, we can manipulate the sublattice detuning parameter Δ. Specifically, for the case of a Γ_2 quench, the objective is to enhance the strength of E_0 to effectively suppress nearest-neighbor (NN) hopping interactions. Simultaneously, a nonzero value of ϕ_i is introduced, which introduces sublattice energy offsets. This introduction of an energy difference between different sublattices leads to the accumulation of a relative phase shift: $a^{\dagger}_{m,n} \to e^{-i\varphi}a^{\dagger}_{m,n}$ and $b^{\dagger}_{m,n} \to e^{i\varphi}b^{\dagger}_{m,n}$. Consequently, this phase alteration leads to changes in the observed pattern within the ToF image.

Just as we assume when introducing the g term, if we can achieve control over spin at the single-site level, we could manipulate the phase difference and achieve quenching in Γ_{13} and Γ_{14}.

In the case of Γ_{12}, we require an additional dimerized optical lattice along one direction. This lattice can be achieved by introducing laser imbalance,

$$\begin{aligned} \mathcal{E}_1(\mathbf{r},t) &= \beta E_0 e^{i(\mathbf{k}_1\cdot\mathbf{r}-\phi_1)-i\omega_L t}\mathbf{e}_x \\ \mathcal{E}_2(\mathbf{r},t) &= -E_0 e^{i(\mathbf{k}_2\cdot\mathbf{r}-\phi_2)-i\omega_L t}\left(\frac{1}{2}\mathbf{e}_x - \frac{\sqrt{3}}{2}\mathbf{e}_y\right) \\ \mathcal{E}_3(\mathbf{r},t) &= -E_0 e^{i(\mathbf{k}_3\cdot\mathbf{r}-\phi_3)-i\omega_L t}\left(\frac{1}{2}\mathbf{e}_x + \frac{\sqrt{3}}{2}\mathbf{e}_y\right). \end{aligned} \tag{F2}$$

By choosing the appropriate β, we can inhibit hopping along two directions and maintain the intersublattice hopping term. Further periodic driving can control the complex tunneling amplitude between sublattices. The tight-binding quench Hamiltonian with effective magnetic field we realized is

$$\begin{aligned} H = &\left(\sum_{m,n,\sigma} J_{AB} e^{i\phi_{AB}} a^{\dagger}_{m,n,\sigma} b_{m,n,\sigma} + \mathrm{H.c.}\right) \\ &+ \Delta\sum_{m,n}\left(a^{\dagger}_{m,n,\uparrow}a_{m,n,\uparrow} - a^{\dagger}_{m,n,\downarrow}a_{m,n,\downarrow}\right) \\ &+ \Delta\sum_{m,n}\left(b^{\dagger}_{m,n,\downarrow}b_{m,n,\downarrow} - b^{\dagger}_{m,n,\uparrow}b_{m,n,\uparrow}\right) \end{aligned} \tag{F3}$$

and its Bloch Hamiltonian is

$$\begin{aligned} H(\mathbf{k}) = &\Delta\Gamma_{15} + J_{AB}\cos(\mathbf{k}\cdot\mathbf{e}_{ab} - \phi_{AB})\Gamma_1 \\ &+ J_{AB}\sin(\mathbf{k}\cdot\mathbf{e}_{ab} - \phi_{AB})\Gamma_{12}, \end{aligned} \tag{F4}$$

where $\mathbf{e}_{ab} = \mathbf{r}_a - \mathbf{r}_b$. The momentum-dependent Hamiltonian gives rise to an evolution operator $U(\mathbf{k},t) = \exp[-iH(\mathbf{k})t]$:

$$\begin{aligned} U(\mathbf{k},t) = &\cos(\widetilde{J}t)\Gamma_0 - i\frac{B}{2\widetilde{J}}\sin(\widetilde{J}t)\Gamma_{15} \\ &- i\frac{J_{AB}}{2\widetilde{J}}\cos(\mathbf{k}\cdot\mathbf{e}_{ab} - \phi_{AB})\sin(\widetilde{J}t)\Gamma_1 \\ &- i\frac{J_{AB}}{2\widetilde{J}}\sin(\mathbf{k}\cdot\mathbf{e}_{ab} - \phi_{AB})\sin(\widetilde{J}t)\Gamma_{12}, \end{aligned} \tag{F5}$$

where $\widetilde{J} = \sqrt{J_{AB}^2 + \Delta^2}/2$ that exhibits a momentum $\mathbf{k}$-dependent quench. For fixed $\mathbf{k}$ results, the $\mathbf{k}$-independent result $\langle\Gamma_{12}\rangle$ can be obtained by setting $(\mathbf{k}\cdot\mathbf{e}_{ab} - \phi_{AB}) = \pi/2$

and the theoretical ToF image is

$$n_{\mathrm{ToF}}(t) = \langle \Gamma_0 \rangle + \cos(4\widetilde{J}t)\langle \Gamma_1 \rangle + \frac{J_{AB}}{2\widetilde{J}} \sin(4\widetilde{J}t)\langle \Gamma_{13} \rangle , \tag{F6}$$

and the $\langle \Gamma_{13} \rangle$ part can be extracted by setting $\widetilde{J}t = \pi/8$. At each step, we can retain only the data from one column with momentum $s\mathbf{k}_\perp$ perpendicular to $\mathbf{e}_{ab}$ to obtain the ToF image.

[1] M. Z. Hasan and C. L. Kane, Colloquium: Topological insulators, Rev. Mod. Phys. **82**, 3045 (2010).

[2] X.-L. Qi and S.-C. Zhang, Topological insulators and superconductors, Rev. Mod. Phys. **83**, 1057 (2011).

[3] B. A. Bernevig and S.-C. Zhang, Quantum spin Hall effect, Phys. Rev. Lett. **96**, 106802 (2006).

[4] H. Weimer, M. Müller, I. Lesanovsky, P. Zoller, and H. P. Büchler, A Rydberg quantum simulator, Nat. Phys. **6**, 382 (2010).

[5] J. T. Barreiro, M. Müller, P. Schindler, D. Nigg, T. Monz, M. Chwalla, M. Hennrich, C. F. Roos, P. Zoller, and R. Blatt, An open-system quantum simulator with trapped ions, Nature (London) **470**, 486 (2011).

[6] S.-L. Zhu, C. Monroe, and L.-M. Duan, Trapped ion quantum computation with transverse phonon modes, Phys. Rev. Lett. **97**, 050505 (2006).

[7] Y. Nakamura, Y. A. Pashkin, and J. S. Tsai, Coherent control of macroscopic quantum states in a single-Cooper-pair box, Nature (London) **398**, 786 (1999).

[8] T. Kitagawa, M. A. Broome, A. Fedrizzi, M. S Rudner, E. Berg, I. Kassal, A. Aspuru-Guzik, E. Demler, and A. G. White, Observation of topologically protected bound states in photonic quantum walks, Nat. Commun. **3**, 882 (2012).

[9] I. Bloch, J. Dalibard, and W. Zwerger, Many-body physics with ultracold gases, Rev. Mod. Phys. **80**, 885 (2008).

[10] M. Lewenstein, A. Sanpera, V. Ahufinger, B. Damski, A. Sen, and U. Sen, Ultracold atomic gases in optical lattices: Mimicking condensed matter physics and beyond, Adv. Phys. **56**, 243 (2007).

[11] D.-W. Zhang, Y.-Q. Zhu, Y. X. Zhao, H. Yan, and S.-L. Zhu, Topological quantum matter with cold atoms, Adv. Phys. **67**, 253 (2018).

[12] A. L. Fetter, Rotating trapped Bose-Einstein condensates, Rev. Mod. Phys. **81**, 647 (2009).

[13] A. S. Sørensen, E. Demler, and M. D. Lukin, Fractional quantum Hall states of atoms in optical lattices, Phys. Rev. Lett. **94**, 086803 (2005).

[14] L.-K. Lim, C. M. Smith, and A. Hemmerich, Staggered-vortex superfluid of ultracold bosons in an optical lattice, Phys. Rev. Lett. **100**, 130402 (2008).

[15] L.-K. Lim, A. Lazarides, A. Hemmerich, and C. M. Smith, Competing pairing states for ultracold fermions in optical lattices with an artificial staggered magnetic field, Phys. Rev. A **82**, 013616 (2010).

[16] T. Kitagawa, E. Berg, M. Rudner, and E. Demler, Topological characterization of periodically driven quantum systems, Phys. Rev. B **82**, 235114 (2010).

[17] F. Mei, S.-L. Zhu, Z.-M. Zhang, C. H. Oh, and N. Goldman, Simulating Z_2 topological insulators with cold atoms in a one-dimensional optical lattice, Phys. Rev. A **85**, 013638 (2012).

[18] J. Dalibard, F. Gerbier, G. Juzeliūnas, and P. Öhberg, Colloquium: Artificial gauge potentials for neutral atoms, Rev. Mod. Phys. **83**, 1523 (2011).

[19] Y.-J. Lin, R. L. Compton, K. Jiménez-García, J. V. Porto, and I. B. Spielman, Synthetic magnetic fields for ultracold neutral atoms, Nature (London) **462**, 628 (2009).

[20] Y.-J. Lin, K. Jiménez-García, and I. B. Spielman, Spin-orbit-coupled Bose-Einstein condensates, Nature (London) **471**, 83 (2011).

[21] S.-L. Zhu, L.-B. Shao, Z. D. Wang, and L.-M. Duan, Probing non-Abelian statistics of Majorana fermions in ultracold atomic superfluid, Phys. Rev. Lett. **106**, 100404 (2011).

[22] Y.-J. Lin, R. L. Compton, A. R. Perry, W. D. Phillips, J. V. Porto, and I. B. Spielman, Bose-Einstein condensate in a uniform light-induced vector potential, Phys. Rev. Lett. **102**, 130401 (2009).

[23] M. Aidelsburger, M. Atala, S. Nascimbène, S. Trotzky, Y.-A. Chen, and I. Bloch, Experimental realization of strong effective magnetic fields in an optical lattice, Phys. Rev. Lett. **107**, 255301 (2011).

[24] K. Osterloh, M. Baig, L. Santos, P. Zoller, and M. Lewenstein, Cold atoms in non-Abelian gauge potentials: From the Hofstadter "moth" to lattice gauge theory, Phys. Rev. Lett. **95**, 010403 (2005).

[25] J.-Z. Li, C.-J. Zou, Y.-X. Du, Q.-X. Lv, W. Huang, Z.-T. Liang, D.-W. Zhang, H. Yan, S. Zhang, and S.-L. Zhu, Synthetic topological vacua of Yang-Mills fields in Bose-Einstein condensates, Phys. Rev. Lett. **129**, 220402 (2022).

[26] D. Jaksch and P. Zoller, Creation of effective magnetic fields in optical lattices: the Hofstadter butterfly for cold neutral atoms, New J. Phys. **5**, 56 (2003).

[27] F. Gerbier and J. Dalibard, Gauge fields for ultracold atoms in optical superlattices, New J. Phys. **12**, 033007 (2010).

[28] N. Goldman, A. Kubasiak, A. Bermudez, P. Gaspard, M. Lewenstein, and M. A. Martin-Delgado, Non-Abelian optical lattices: Anomalous quantum Hall effect and Dirac fermions, Phys. Rev. Lett. **103**, 035301 (2009).

[29] S.-L. Zhu, H. Fu, C.-J. Wu, S.-C. Zhang, and L.-M. Duan, Spin Hall effects for cold atoms in a light-induced gauge potential, Phys. Rev. Lett. **97**, 240401 (2006).

[30] M.-C. Liang, Y.-D. Wei, L. Zhang, X.-J. Wang, H. Zhang, W.-W. Wang, W. Qi, X.-J. Liu, and X. Zhang, Realization of Qi-Wu-Zhang model in spin-orbit-coupled ultracold fermions, Phys. Rev. Res. **5**, L012006 (2023).

[31] N. Goldman and P. Gaspard, Quantum Hall-like effect for cold atoms in non-Abelian gauge potentials, Europhys. Lett. **78**, 60001 (2007).

[32] L. B. Shao, S.-L. Zhu, L. Sheng, D. Y. Xing, and Z. D. Wang, Realizing and detecting the quantum Hall effect without Landau levels by using ultracold atoms, Phys. Rev. Lett. **101**, 246810 (2008).

[33] C. Wu, Orbital analogue of the quantum anomalous Hall effect in p-band systems, Phys. Rev. Lett. **101**, 186807 (2008).

[34] T. D. Stanescu, V. Galitski, J. Y. Vaishnav, C. W. Clark, and S. Das Sarma, Topological insulators and metals in atomic optical lattices, Phys. Rev. A **79**, 053639 (2009).

[35] E. Alba, X. Fernandez-Gonzalvo, J. Mur-Petit, J. K. Pachos, and J. J. Garcia-Ripoll, Seeing topological order in time-of-flight measurements, Phys. Rev. Lett. **107**, 235301 (2011).

[36] B. Béri and N. R. Cooper, $\mathbb{Z}_2$ topological insulators in ultracold atomic gases, Phys. Rev. Lett. **107**, 145301 (2011).

[37] N. Goldman, I. Satija, P. Nikolic, A. Bermudez, M. A. Martin-Delgado, M. Lewenstein, and I. B. Spielman, Realistic time-reversal invariant topological insulators with neutral atoms, Phys. Rev. Lett. **105**, 255302 (2010).

[38] M. Atala, M. Aidelsburger, J. T. Barreiro, D. Abanin, T. Kitagawa, E. Demler, and I. Bloch, Direct measurement of the Zak phase in topological Bloch bands, Nat. Phys. **9**, 795 (2013).

[39] L. Duca, T. Li, M. Reitter, I. Bloch, M. Schleier-Smith, and U. Schneider, An Aharonov-Bohm interferometer for determining Bloch band topology, Science **347**, 288 (2015).

[40] F. Grusdt, N. Y. Yao, D. Abanin, M. Fleischhauer, and E. Demler, Interferometric measurements of many-body topological invariants using mobile impurities, Nat. Commun. **7**, 11994 (2016).

[41] D. A. Abanin, T. Kitagawa, I. Bloch, and E. Demler, Interferometric approach to measuring band topology in 2D optical lattices, Phys. Rev. Lett. **110**, 165304 (2013).

[42] F. Grusdt, D. Abanin, and E. Demler, Measuring $\mathbb{z}_2$ topological invariants in optical lattices using interferometry, Phys. Rev. A **89**, 043621 (2014).

[43] H. M. Price and N. R. Cooper, Mapping the Berry curvature from semiclassical dynamics in optical lattices, Phys. Rev. A **85**, 033620 (2012).

[44] A. Dauphin and N. Goldman, Extracting the Chern number from the dynamics of a Fermi gas: Implementing a quantum Hall bar for cold atoms, Phys. Rev. Lett. **111**, 135302 (2013).

[45] G. Jotzu, M. Messer, R. Desbuquois, M. Lebrat, T. Uehlinger, D. Greif, and T. Esslinger, Experimental realization of the topological Haldane model with ultracold fermions, Nature (London) **515**, 237 (2014).

[46] M. Aidelsburger, M. Lohse, C. Schweizer, M. Atala, J. T. Barreiro, S. Nascimbène, N. R. Cooper, I. Bloch, and N. Goldman, Measuring the Chern number of Hofstadter bands with ultracold bosonic atoms, Nat. Phys. **11**, 162 (2015).

[47] T. Szołdra, K. Sacha, and A. Kosior, Determination of Chern numbers with a phase-retrieval algorithm, Phys. Rev. A **99**, 043611 (2019).

[48] D.-L. Deng, S.-T. Wang, and L.-M. Duan, Direct probe of topological order for cold atoms, Phys. Rev. A **90**, 041601(R) (2014).

[49] P. Hauke, M. Lewenstein, and A. Eckardt, Tomography of band insulators from quench dynamics, Phys. Rev. Lett. **113**, 045303 (2014).

[50] N. Fläschner, B. S. Rem, M. Tarnowski, D. Vogel, D.-S. Lühmann, K. Sengstock, and C. Weitenberg, Experimental reconstruction of the Berry curvature in a Floquet Bloch band, Science **352**, 1091 (2016).

[51] C.-R. Yi, J. Yu, H. Yuan, R.-H. Jiao, Y.-M. Yang, X. Jiang, J.-Y. Zhang, S. Chen, and J.-W. Pan, Extracting the quantum geometric tensor of an optical Raman lattice by Bloch-state tomography, Phys. Rev. Res. **5**, L032016 (2023).

[52] T. Li, L. Duca, M. Reitter, F. Grusdt, E. Demler, M. Endres, M. Schleier-Smith, I. Bloch, and U. Schneider, Bloch state tomography using wilson lines, Science **352**, 1094 (2016).

[53] M. Tarnowski, M. Nuske, N. Fläschner, B. Rem, D. Vogel, L. Freystatzky, K. Sengstock, L. Mathey, and C. Weitenberg, Observation of topological Bloch-state defects and their merging transition, Phys. Rev. Lett. **118**, 240403 (2017).

[54] P. Streda, Theory of quantised Hall conductivity in two dimensions, J. Phys. C **15**, L717 (1982).

[55] R. O. Umucalılar, H. Zhai, and M. Ö. Oktel, Trapped Fermi gases in rotating optical lattices: Realization and detection of the topological Hofstadter insulator, Phys. Rev. Lett. **100**, 070402 (2008).

[56] S.-L. Zhu, Z.-D. Wang, Y.-H. Chan, and L.-M. Duan, Topological Bose-Mott insulators in a one-dimensional optical superlattice, Phys. Rev. Lett. **110**, 075303 (2013).

[57] E. Zhao, N. Bray-Ali, C. J. Williams, I. B. Spielman, and I. I. Satija, Chern numbers hiding in time-of-flight images, Phys. Rev. A **84**, 063629 (2011).

[58] F. Li, L. B. Shao, L. Sheng, and D. Y. Xing, Simulation of the quantum Hall effect in a staggered modulated magnetic field with ultracold atoms, Phys. Rev. A **78**, 053617 (2008).

[59] L.-J. Lang, X. Cai, and S. Chen, Edge states and topological phases in one-dimensional optical superlattices, Phys. Rev. Lett. **108**, 220401 (2012).

[60] D.-W. Zhang, L.-Z. Tang, L.-J. Lang, H. Yan, and S.-L. Zhu, Non-Hermitian topological Anderson insulators, Sci. China Phys. Mech. Astron. **63**, 267062 (2020).

[61] X.-J. Liu, X. Liu, C. Wu, and J. Sinova, Quantum anomalous Hall effect with cold atoms trapped in a square lattice, Phys. Rev. A **81**, 033622 (2010).

[62] N. Goldman, J. Beugnon, and F. Gerbier, Detecting chiral edge states in the Hofstadter optical lattice, Phys. Rev. Lett. **108**, 255303 (2012).

[63] T. D. Stanescu, V. Galitski, and S. Das Sarma, Topological states in two-dimensional optical lattices, Phys. Rev. A **82**, 013608 (2010).

[64] M. Buchhold, D. Cocks, and W. Hofstetter, Effects of smooth boundaries on topological edge modes in optical lattices, Phys. Rev. A **85**, 063614 (2012).

[65] M. Killi and A. Paramekanti, Use of quantum quenches to probe the equilibrium current patterns of ultracold atoms in an optical lattice, Phys. Rev. A **85**, 061606(R) (2012).

[66] M. D. Reichl and E. J. Mueller, Floquet edge states with ultracold atoms, Phys. Rev. A **89**, 063628 (2014).

[67] S.-L. Zhu, B. Wang, and L.-M. Duan, Simulation and detection of Dirac fermions with cold atoms in an optical lattice, Phys. Rev. Lett. **98**, 260402 (2007).

[68] C. J. Kennedy, G. A. Siviloglou, H. Miyake, W. C. Burton, and W. Ketterle, Spin-orbit coupling and quantum spin Hall effect for neutral atoms without spin flips, Phys. Rev. Lett. **111**, 225301 (2013).

[69] M. Aidelsburger, M. Atala, M. Lohse, J. T. Barreiro, B. Paredes, and I. Bloch, Realization of the Hofstadter Hamiltonian with ultracold atoms in optical lattices, Phys. Rev. Lett. **111**, 185301 (2013).

[70] C. L. Kane and E. J. Mele, Z_2 topological order and the quantum spin Hall effect, Phys. Rev. Lett. **95**, 146802 (2005).

[71] D. N. Sheng, Z. Y. Weng, L. Sheng, and F. D. M. Haldane, Quantum spin-Hall effect and topologically

invariant Chern numbers, Phys. Rev. Lett. **97**, 036808 (2006).

[72] H. Li, L. Sheng, D. N. Sheng, and D. Y. Xing, Chern number of thin films of the topological insulator Bi_2Se_3, Phys. Rev. B **82**, 165104 (2010).

[73] F. D. M. Haldane, Berry curvature on the Fermi surface: Anomalous Hall effect as a topological Fermi-liquid property, Phys. Rev. Lett. **93**, 206602 (2004).

[74] E. Prodan, Robustness of the spin-Chern number, Phys. Rev. B **80**, 125327 (2009).

[75] Q.-X. Lv, Y.-X. Du, Z.-T. Liang, H.-Z. Liu, J.-H. Liang, L.-Q. Chen, L.-M. Zhou, S.-C. Zhang, D.-W. Zhang, B.-Q. Ai, H. Yan, and S.-L. Zhu, Measurement of spin Chern numbers in quantum simulated topological insulators, Phys. Rev. Lett. **127**, 136802 (2021).

[76] Y. Yang, Z. Xu, L. Sheng, B. Wang, D. Y. Xing, and D. N. Sheng, Time-reversal-symmetry-broken quantum spin Hall effect, Phys. Rev. Lett. **107**, 066602 (2011).

[77] D.-W. Zhang, Y. X. Zhao, R.-B. Liu, Z.-Y. Xue, S.-L. Zhu, and Z. D. Wang, Quantum simulation of exotic PT-invariant topological nodal loop bands with ultracold atoms in an optical lattice, Phys. Rev. A **93**, 043617 (2016).

[78] P. Soltan-Panahi, J. Struck, P. Hauke, A. Bick, W. Plenkers, G. Meineke, C. Becker, P. Windpassinger, M. Lewenstein, and K. Sengstock, Multi-component quantum gases in spin-dependent hexagonal lattices, Nat. Phys. **7**, 434 (2011).

[79] K. L. Lee, B. Grémaud, R. Han, B.-G. Englert, and C. Miniatura, Ultracold fermions in a graphene-type optical lattice, Phys. Rev. A **80**, 043411 (2009).

[80] J. Struck, C. Ölschläger, M. Weinberg, P. Hauke, J. Simonet, A. Eckardt, M. Lewenstein, K. Sengstock, and P. Windpassinger, Tunable gauge potential for neutral and spinless particles in driven optical lattices, Phys. Rev. Lett. **108**, 225304 (2012).

[81] P. Hauke, O. Tieleman, A. Celi, C. Ölschläger, J. Simonet, J. Struck, M. Weinberg, P. Windpassinger, K. Sengstock, M. Lewenstein, and A. Eckardt, Non-Abelian gauge fields and topological insulators in shaken optical lattices, Phys. Rev. Lett. **109**, 145301 (2012).

[82] W. Zheng and H. Zhai, Floquet topological states in shaking optical lattices, Phys. Rev. A **89**, 061603(R) (2014).

[83] F. Großmann and P. Hänggi, Localization in a driven two-level dynamics, Europhys. Lett. **18**, 571 (1992)

[84] D. H. Dunlap and V. M. Kenkre, Dynamic localization of a charged particle moving under the influence of an electric field, Phys. Rev. B **34**, 3625 (1986).

[85] M. Holthaus, Collapse of minibands in far-infrared irradiated superlattices, Phys. Rev. Lett. **69**, 351 (1992).

[86] A. Eckardt, C. Weiss, and M. Holthaus, Superfluid-insulator transition in a periodically driven optical lattice, Phys. Rev. Lett. **95**, 260404 (2005).

[87] E. Kierig, U. Schnorrberger, A. Schietinger, J. Tomkovic, and M. K. Oberthaler, Single-particle tunneling in strongly driven double-well potentials, Phys. Rev. Lett. **100**, 190405 (2008).

[88] A. Zenesini, H. Lignier, D. Ciampini, O. Morsch, and E. Arimondo, Coherent control of dressed matter waves, Phys. Rev. Lett. **102**, 100403 (2009).

[89] J. Struck, C. Ölschläger, R. L. Targat, P. Soltan-Panahi, A. Eckardt, M. Lewenstein, P. Windpassinger, and K. Sengstock, Quantum simulation of frustrated classical magnetism in triangular optical lattices, Science **333**, 996 (2011).

[90] K. Sacha, K. Targońska, and J. Zakrzewski, Frustration and time-reversal symmetry breaking for Fermi and Bose-Fermi systems, Phys. Rev. A **85**, 053613 (2012).

[91] J.-T. Wang, J.-X. Liu, H.-T. Ding, and P. He, Proposal for implementing Stiefel-Whitney insulators in an optical Raman lattice, Phys. Rev. A **109**, 053314 (2024).

[92] T. Fukui, Y. Hatsugai, and H. Suzuki, Chern numbers in discretized Brillouin zone: Efficient method of computing (spin) Hall conductances, J. Phys. Soc. Jpn. **74**, 1674 (2005).

[93] N. Goldman and J. Dalibard, Periodically driven quantum systems: Effective Hamiltonians and engineered gauge fields, Phys. Rev. X **4**, 031027 (2014).